Nanoscale

Phase-Dependent Shear-Induced Order of Nanorods in Isotropic and Nematic Wormlike Micelle Solutions

Journal:	*Nanoscale*
Manuscript ID	NR-ART-12-2018-010440.R2
Article Type:	Paper
Date Submitted by the Author:	28-Mar-2019
Complete List of Authors:	Mhanna, Ramona; Johns Hopkins University Lee, Jonghun; Argonne National Laboratory Narayanan, Suresh; Argonne National Laboratory Reich, Daniel; Johns Hopkins University, Physics and Astronomy Leheny, Robert; Johns Hopkins University, Physics and Astronomy

Phase-Dependent Shear-Induced Order of Nanorods in Isotropic and Nematic Wormlike Micelle Solutions

Ramona Mhanna[1], Jonghun Lee[2], Suresh Narayanan[2], Daniel H. Reich[1], Robert L. Leheny[1,*]

[1]Department of Physics & Astronomy, Johns Hopkins University, Baltimore, MD 21218, USA.

[2]X-Ray Science Division, Argonne National Laboratory, Lemont, IL 60439, USA.

[*]leheny@jhu.edu

Small angle x-ray scattering with *in situ* shear was employed to study the assembly and ordering of dispersions of gold nanorods within wormlike micelle solutions formed by the surfactant cetylpyridinium chloride (CPyCl) and counter-ion sodium salicylate (NaSal). Above a threshold CPyCl concentration but below the isotropic-to-nematic transition of the micelles, the nanorods self-assembled under quiescent conditions into isotropically oriented domains with hexagonal order. Under steady shear at rates between 0.5 and 7.5 s^{-1}, the nanorod assemblies acquired macroscopic orientational order in which the hexagonal planes were coincident with the flow-vorticity plane. The nanorods could be re-dispersed by strong shear but re-assembled following cessation of the shear. In the nematic phase of the micelles at higher surfactant concentration, the nanorods did not acquire hexagonal order but instead formed smectic-like layers in the gradient-vorticity plane under shear. Finally, at still higher surfactant concentration, where the micelles form a hexagonal phase, the nanorods showed no translational ordering but did acquire nematic-like order under shear due to alignment in the flow. Depletion forces mediated by the wormlike micelles are identified as the driving mechanism for this sequence of nanorod ordering behaviors, suggesting a novel mechanism for controlled, reconfigurable assembly of nanoparticles in solution.

I. Introduction

Strategies for the formation of ordered assemblies of nanoparticles are important for engineering new materials and devices that leverage the particles' unique properties. Making uniform assemblies over a large volume is essential to many potential applications, for example for realizing many electronic,[1] optical,[2] and high-density data storage[3] applications. Furthermore, the ability to template different ordered structures provides a mechanism to alter nanoparticles' collective physical properties.[2, 4] The assembly of rod-shaped nanoparticles holds special interest due to the particular electronic and optical properties of nanorods that make them promising fundamental building blocks for applications in areas such as optoelectronics, sensing, and plasmonics.[5-11]

A well studied approach for the assembly of nanoparticles from solution involves solvent evaporation, which typically leads to close packed structures.[3, 12-14] However, this process is simultaneously sensitive to a range of parameters, such as solvent vapor pressure, temperature, and humidity, that makes outcomes difficult to control, and high-quality assemblies are often achieved only in a narrow range of conditions. Tailoring the interactions between nanoparticles in solution can improve control over assembly. An example of this strategy involves depletion forces that are created when polymers or surfactants are introduced into nanoparticle suspensions. These additives induce an attraction between the nanoparticles due to the creation of an osmotic pressure imbalance around nanoparticles in close proximity, and this depletion force can direct monodisperse nanoparticles to assemble into ordered structures.[15-18] Enhanced control of assembly can also be achieved through the application of external forces to nanoparticles in solution.[19, 20] For example, introducing a flow field, such as by spin coating or by oscillatory shear, can facilitate assembly.[21-23] Here, we report a study of the self-assembly and ordering behavior of gold nanorods that employs both depletion forces and flow by suspending the nanorods in wormlike micelle (WLM) solutions that we subject to shear. Wormlike micelles are long, thin assemblies of surfactant molecules that form under appropriate conditions in aqueous solution and that possess similarities to polymers. However, unlike polymers, WLMs are governed by weak electrostatic interactions rather than chemical bonds, which allow them to break and re-assemble. They are, therefore, referred to as "living" polymers. These properties give WLM solutions characteristic linear and nonlinear rheology[24-26]. At sufficient concentration,

WLMs can entangle, leading to viscoelastic solutions, and can form ordered phases in which the micelles display nematic or hexagonal order.[25] Importantly, like polymers, WLMs have been shown to mediate depletion forces that can lead to colloidal aggregation, pointing to their potential application in controlled nanoparticle assembly.[27, 28]

In this paper we present results that combine small-angle x-ray scattering (SAXS) with *in situ* shear to demonstrate how interactions mediated by WLMs in conjunction with shear are capable of driving gold nanorods into assemblies with order that extends over macroscopic scales. SAXS is well suited to characterize nanometer-scale structures, including nanoparticle assemblies.[29] Compared with scanning electron microscopy and transmission electron microscopy, SAXS can easily measure liquid-phase samples, and it exhibits higher temporal resolution, which is important to resolving structural changes in nanorod dispersions induced by shear stress. In particular, a combination of SAXS and rheology has provided a unique *in situ* method to observe the shear-induced structure formation in nanoparticle suspensions and related systems.[30, 31]

The nature of the ordering of the nanorods in the WLM solutions is sensitive to the phase of the WLMs, which changes from isotropic to nematic to hexagonal as a function of surfactant concentration.[25] In isotropic solutions of WLMs, the rods form close packed crystal structures whose hexagonal planes assume long-range orientational order with respect to the shear flow. In contrast, in the nematic phase of the WLMs, the nanorods adopt an ordering that resembles a smectic liquid crystal, while in the hexagonal phase of the micelles, the nanorods align under shear but show no long-range translational order. Depletion forces mediated by the WLMs are identified as the primary mechanism driving the nanorod assembly. The sensitivity of the ordering behavior to the WLM phase, along with other distinct features of WLM solutions, indicate these forces can serve as the basis for controlled, reconfigurable assembly of nanoparticles in solution.

II. Materials and Methods

The study focused on gold nanorods suspended in solutions of the surfactant cetylpyridinium chloride (CPyCl, $(C_{16}H_{33})$-(C_5H_5)-N^+Cl^-) and the counterion sodium salicylate (NaSal, $C_7H_5NaO_3$), a well-studied system that forms polyelectrolyte WLMs over a broad range of surfactant concentration.

A. Synthesis of Gold Nanorods

The gold nanorods were synthesized using seed-mediated growth in aqueous solutions of cetyltrimethylammonium bromide (CTAB; TCI America) following procedures reported by Ye *et al*.[14] The nanorods had radius $R = 7.5 \pm 0.8$ nm and length $L = 75.0 \pm 4.4$ nm, as determined by transmission electron microscopy. (See Fig. S1 in the Supplementary Information.) Initially, the nanorods were stabilized in the water by excess CTAB that coated the particle surfaces. Upon mixing with CPyCl/NaSal, CTAB loses affinity to the gold surfaces in the presence of the salicylate ions, leading to aggregation of the nanorods. Therefore, the nanorods were functionalized with methoxy poly(ethylene glycol) thiol (mPEG-SH; Creative PEGWorks) with molecular weight of 2000 g/mol prior to their introduction into the WLM solutions. For this functionalization, CTAB-coated nanorods were centrifuged at $4000 \times g$ for 25 min twice to remove excess CTAB and then were mixed with 2 mM mPEG-SH aqueous solution for 24 h. Any remaining CTAB and unreacted mPEG-SH were then removed by multiple centrifugations. The nanorods functionalized with mPEG were found to remain stable in deionized water for several months. (See Fig. S2 in the Supplementary Information, showing the small angle x-ray scattering intensity from such a solution, which resembles the lineshape of the form factor of isolated rods averaged over orientation.)

B. WLM Solutions

Desired quantities of CPyCl (Alfa Aesar) and NaSal (Alfa Aesar) were added to dilute stock solutions of the mPEG-functionalized nanorods to prepare WLM solutions with varying micelle concentrations. From the absolute scattering intensity in the x-ray scattering experiments, the volume fraction of rods was estimated to be ~0.01%. This concentration was sufficiently low so as not to affect the rheological properties of the WLM solutions. However,

despite this low volume fraction the nanorods dominated the SAXS measurements due to the large atomic number of gold. A series of five WLM solutions with CPyCl concentrations c = 110 mM , 220 mM, 400 mM, 1,133 mM, and 1,500 mM were prepared. At the lowest three concentrations the WLMs form an isotropic, entangled solution, while at c = 1,133 mM, the micelles order in a nematic phase, and at c = 1,500 mM, they form a hexagonal phase.[25] At fixed CPyCl concentration, the viscosity of CPyCl/NaSal solutions shows two maxima as a function of NaSal concentration.[32] At salt concentrations below the first maximum, increasing salt is thought to increase the average micelle length, leading to increasingly entangled solutions, while above the first maximum, the micelles are thought to develop a branched morphology that facilitates stress relaxation.[25, 33] In the solutions in this study, we maintained the molar ratio of NaSal to CPyCl coincident with the first viscosity maximum. Specifically, we followed the relation between c and NaSal concentration c_s at the first viscosity maximum identified by Rehage and Hoffmann: $\log(c_s/\text{mM}) = 0.23 + 0.8\log(c/\text{mM})$.[32] Hence, for each CPyCl concentration the solutions contained micelles that were as long as possible without significant branching. The WLM solutions also displayed shear thinning under steady shear above shear rates of $\dot{\gamma} \approx 1$ s^{-1}. Fig. S3 in the Supplementary Information shows results for the effective viscosity as a function of shear rate of a set of solutions with varying surfactant concentrations.

C. SAXS Measurements

The SAXS experiments under *in situ* shear were performed at Sector 8-ID of the Advanced Photon Source. Solutions were contained in a polycarbonate Couette cell with 0.2 mm wall thickness, which allowed x-rays to penetrate with little attenuation. The cell height was 15.0 mm, and the inner and outer diameters were 11.0 and 11.4 mm, leading to a cell gap of 0.2 mm. After a sample was loaded into the Couette cell, it was typically subjected to shear at a high rate, $\dot{\gamma}$ = 50 s^{-1}, to eliminate any effects of the loading process. An 11 keV x-ray beam of size 20 × 20 μm^2 was incident on the sample. The SAXS data were collected using direct detection with a charge-coupled device (CCD) detector (Princeton Instruments LCX-1300) with 20 × 20 μm^2 pixel size located 4.91 m behind the sample. By varying the detector position relative to the incident beam, the scattering wave-vector range 0.01 nm^{-1} < q < 1.5 nm^{-1} was covered. Measurements were performed in transmission with the incident beam directed either radially through the center of cell or tangentially through the edge of the cell, as depicted schematically in

Fig. 1. In the small-angle scattering regime of the measurements, when the beam was in the radial configuration the scattering wave vector was in the flow-vorticity (v–ω) plane, while in the tangential configuration it was in the gradient-vorticity (Δ– ω) plane. In a typical measurement, between 64 and 200 CCD images were obtained, with an exposure time of 0.1 s, and the images were summed to produce a SAXS pattern. All measurements were at room temperature. Data analysis was performed using the Nika software package.[34, 35]

III. Results

A. Nanorod ordering in isotropic wormlike micelle solutions

1. Self-assembly under quiescent conditions

At the lowest micelle concentration studied, c = 110 mM, the nanorods remained well dispersed in the WLM solutions over the course of hours. However, at the higher micelle concentrations, *i. e.*, c = 220 mM and above, the SAXS measurements observed the slow assembly and development of local order among the nanorods under quiescent (zero shear) conditions. This order formation is illustrated in Fig. 2, which displays a sequence of SAXS patterns from a solution with c = 400 mM at various times during and following cessation of the pre-shear. The patterns in Fig. 2 were obtained in the radial scattering geometry, as in Fig. 1(b), so that the scattering plane was coincident with the flow-vorticity plane. The SAXS patterns obtained during the pre-shear at 50 s^{-1}, shown in Fig. 2(a), possessed an anisotropic shape characteristic of the form factor of isolated rods aligned with their axes parallel to the flow velocity. Such alignment parallel to the flow direction is expected for prolate particles at high shear rates in complex fluids with sufficient viscoelasticity.[36-38] When the shear flow ceased, the rods quickly lost this alignment, presumably through rotational diffusion, and the SAXS intensity reverted to an isotropic pattern resembling the form factor of a rod averaged over orientations, as illustrated by Fig. 2(b), which displays a pattern obtained two minutes after the cessation of the shear. Left under quiescent conditions, however, the initially dispersed rods in the WLM solution at c = 400 mM steadily assembled, as revealed by a ring of scattering intensity at q = 0.246 nm^{-1} seen in Fig. 2(c) and (d) that grew over the course of tens of minutes. The rate of formation of

the order was characterized by the growth of the azimuthally averaged peak intensity of the ring with time, as shown in Fig. 2(e). This assembly could be destroyed by application of shear at a sufficiently high rate ($\dot{\gamma} > 20$ s^{-1}), which would lead after several minutes of shear to SAXS patterns of dispersed aligned rods like in Fig. 2(a). This destruction by high shear followed by re-emergence of order after flow cessation was repeated as many as four times on a single sample during the experiments, and temporal evolution in the growth of the order was similar each time, indicating that the process could be repeated indefinitely.

2. Shear-induced order

While strong shear ($\dot{\gamma} > 20$ s^{-1}) re-dispersed the assembled rods, shear at moderate rates enhanced the order by inducing long-range orientational correlations among the rods. This ordering is illustrated in Fig. 3(a) and (b), which show SAXS patterns from a solution with c = 400 mM upon application of steady shear at $\dot{\gamma} = 2.5$ s^{-1} for 4 minutes and 78 minutes, respectively. The patterns in Fig. 3(a) and (b) were again obtained in the radial scattering geometry, so that the scattering plane was coincident with the flow-vorticity plane. Upon application of the moderate shear, the isotropic ring of scattering evolved into a set of peaks with six-fold symmetry. Based on this observation, we interpret the ring of scattering that forms under quiescent conditions as a "powder" Bragg peak from randomly oriented assemblies of hexagonally packed rods that assume a common orientation due to the shear.

This long-range hexagonal order appeared almost immediately with the start of the shear, but the quality of the order, as measured by the sharpness of the Bragg peaks, evolved over tens of minutes. This evolution is illustrated in Fig. 3(c), which shows the scattering intensity at the wave-vector magnitude of the peaks ($q = 0.24$ nm^{-1}) as a function of angle ϕ with respect to the flow direction (q_v) in the flow-vorticity plane at 4 min and 78 min after the commencement of shear at $\dot{\gamma} = 2.5$ s^{-1}. Specifically, the plot shows the intensity per pixel averaged over a five-pixel-wide circular band centered at $|q| = 0.24$ nm^{-1}. Such six-fold symmetric patterns were observed for a range of shear rates, $\dot{\gamma} = 0.5 – 7.5$ s^{-1}, with the sharpest peaks forming at $\dot{\gamma} = 2.5 – 5$ s^{-1}. These peaks indicate that the rods in the WLM solution packed side-by-side to form hexagonal lattices that then oriented within the flow-vorticity plane of the shear flow such that the rod axes were parallel to the gradient direction. One lattice vector of the hexagonal lattices was aligned

with the flow direction and the other was oriented at 30º to the vorticity direction. The lattice spacing was $a \approx 30$ nm, or approximately twice the diameter of the rods. With this identification of lattice vectors, the peak parallel to q_ω in Fig. 3(b) and (c) is the (01) peak of the two-dimensional reciprocal lattice, and the peak at 30º to q_v is the (11) peak. The hexagonal packing of the rods in the flow-vorticity plane was further confirmed by SAXS patterns measured with the detector positioned to capture larger wave-vector Bragg peaks, as shown in Fig. 4(a)-(c). The patterns include Bragg peaks at five wave-vector magnitudes 0.24 nm^{-1}, 0.42 nm^{-1}, 0.5 nm^{-1}, 0.65 nm^{-1}, and 0.74 nm^{-1} – with corresponding ratios $1{:}\sqrt{3}{:}2{:}\sqrt{7}{:}3$ – and at relative orientations in the scattering plane consistent with the reciprocal lattice points given by the labels in the figures. Fig. 5(a) schematically depicts the real space orientation of the hexagonal packing with respect to the shear flow.

The quality of the in-plane hexagonal order is obtained from the width of the peaks. Fig. 3(d) shows the scattering intensity from a cut through the (01) peak along with a fit to the peak using a Lorentzian form plus a sloping background,

$$I(q_\omega) = I_0 - S * q_\omega + \frac{A}{(q_\omega - q_0)^2 + \xi^2} \qquad (1)$$

where $q_0 = 0.241$ nm^{-1} is the peak position, A is the peak amplitude, ξ is the correlation length, and I_0 and S characterize the background. The result of the fit gives a correlation length $\xi = 210 \pm 2$ nm, or approximately 7 lattice spacings. A similar fit to the (11) peak gives $\xi = 260 \pm 3$ nm.

This flow-induced orientational ordering of the hexagonally packed nanorods depicted in Fig. 5(a) is strikingly similar to the behavior seen with concentrated spherical colloids with hard-sphere or repulsive interactions that are subject to steady shear flow.[39-41] Specifically, at sufficiently high concentration, (*e.g.*, above a volume fraction of 0.495 for the case of hard spheres), spherical colloids form close-packed crystal structures that become long-range ordered under moderate shear such that the hexagonal planes of the crystals orient with respect to the flow like in Fig. 5(a). In the case of the close-packed spheres, this orientational order is thought to reduce the resistance by the crystals to the flow. [39] A similar effect apparently occurs among the self-assembled rods.

A question regarding this nanorod ordering is whether the hexagonal packings stack to form three-dimensional assemblies, and if so, how the hexagonal planes arrange with respect to one another. In the close-packed lattices formed by dense spheres, the colloids in one layer are positioned above interstitial points of the adjacent layer, with two possible sets of points being selected. For instance, if the particles labeled A in Fig. 5(b) form one layer, then the particles in the next layer in the stacking can be positioned either above the sites marked B or above those marked C. Under quiescent conditions concentrated hard spheres typically form FCC lattices with the stacking sequence ABCABCABC (or equivalently its twin ACBACBACB), but shear flow can modify the stacking arrangement as the lattice strains and the layers slip past one another.[39-42] Evidence for the stacking arrangement of the nanorods comes from the intensities of the peaks in Fig. 3, in which the (01) peak along the vorticity direction is weaker than the (11) peak. This same modulation in peak intensities is seen for crystals of spherical colloids under moderate shear.[39-41] In that case, the behavior has been modeled in terms of random close packed (RCP) structures (*i.e.*, those with a random stacking arrangement) in which the hexagonal layers undergo shear-induced displacements with respect to their neighbors that follow a zig-zag pattern, as depicted by the dashed lines in Fig 5(b).[42] The similarity in the relative peak intensities between those model calculations and the results in Fig. 3 suggests that the hexagonally packed nanorods similarly stack to form a RCP layer structure that is strained by the shear flow.

Further information about the stacking arrangement comes from SAXS measurements performed in the tangential scattering geometry depicted in Fig. 1(b) in which the scattering plane is coincident with the gradient-vorticity plane. Fig. 6(a) and (b) display the scattering intensity on a logarithmic scale measured in this geometry for a solution with c = 400 mM before and during the application of shear at $\dot{\gamma}$ = 2.5 s^{-1}, respectively. Again, the ring of scattering that developed under quiescent conditions was transformed into an anisotropic scattering pattern by the shear. In this scattering geometry, the measurements capture the scattering intensity in the (0KL) plane in reciprocal space of the nanorod lattice with q_{ω} along K and q_{Δ} along L. For a single hexagonal layer, the peaks in the (HK0) plane like those in Fig. 3 and 4 would be "Bragg tubes" of uniform intensity in the L direction. Stacking of the layers leads to modulation in the

intensity of the tubes that depends on the stacking arrangement. The SAXS pattern in Fig. 6(b) captures the intensities along the (00L) and (01L) Bragg tubes.

Fig. 6(c) displays the scattering intensity along each tube. Specifically, the figure shows the intensity per pixel averaged over a ten-pixel-wide horizontal band centered at $q_\omega = 0$ for the (00L) tube and $q_\omega = 0.24$ nm^{-1} for the (01L) tube and multiplied by q_Δ^2 to correct approximately for the form factor of rods aligned along the gradient direction. For the case of a (unstrained) RCP structure, the intensity along (00L) is comprised of a set of Bragg peaks at integer values of L, while the intensity along (01L) is diffuse but modulated with maxima at L=(n+1/2), where n is an integer. For an RCP structure that is undergoing strain corresponding to displacements of nearest neighbor layers along the zig-zag trajectories shown in Fig. 5(b), intensity along the (01L) tube is altered in a way that depends on the displacements.[42] The (01L) tube intensity in Fig. 6(c) appears to share features of the RCP structure, with two peaks visible with periodicity of approximately $\Delta q \approx 0.087$ nm^{-1} that could be identified as the L=3/2 and L=5/2 positions, implying a lattice spacing along the stacking direction, $2\pi/\Delta q \approx 72$ nm. Since this spacing is slightly smaller than the average rod length, it implies inter-digitation of the hexagonal layers, a conclusion that is consistent with an RCP structure and is supported by the measured hexagonal lattice vector, a ≈ 30 nm, being twice the rod diameter.

However, this identification is complicated by the measured intensity along the (00L) direction, which does not contain clear Bragg peaks expected for a well-ordered RCP lattice but instead is diffuse with intensity modulations that indicate short-range order. Such limited, short-range order in the layering is consistent with what one might expect given the polydispersity in rod length and the shear-induced strain. Hence, from these observations we tentatively conclude that the rod assemblies in the isotropic WLM micelle solutions under shear were composed of hexagonal layers of rods in the flow-vorticity plane that were stacked such that adjacent layers had lateral correlations consistent with an RCP structure under strain due to the shear flow but a layer spacing that was only short-range ordered.

An important difference between the nanorods and concentrated hard spheres that form close packed structures was that the rods were in dilute suspension, and their assemblies into ordered lattices hence must be driven by attractive interactions (discussed further in Sec. III.C

below). Consequently, the nanorod assemblies were not space filling, and the rods presumably formed a population of crystallites in solution. The intensity of the SAXS patterns like in Fig. 3, 4, and 6 were highly uniform as the position of the beam was varied within the sample, indicating that the crystallites were uniformly dispersed macroscopically. Information about the shape of the crystallites can be inferred from the low-q scattering in Fig. 6(b), which we associate with the form factor of the crystallites. The anisotropic shape of the low-q scattering, with intensity that extends to higher wave vector along q_Δ than along q_ω, implies that the crystallites had a prolate shape in which they were more extended in the vorticity direction than in the gradient direction. That is, the hexagonally packed sheets of rods were larger than the extent of the stacking.

The long-range hexagonal order at moderate shear rates implied by the six-fold symmetry of the scattering in Fig. 3 and 4 can thus be interpreted as a result of the crystallites in suspension assuming a common orientation under the shear. At lower shear rates ($\dot{\gamma} < 0.5$ s^{-1}), the powder ring that formed under quiescent conditions did not develop these signature six-fold peaks, but instead acquired a two-fold anisotropy in intensity, as illustrated in Fig. 7(a) and (b), which show the scattering pattern from a solution with c = 400 mM upon application of steady shear at $\dot{\gamma}$ = 0.1 s^{-1} in the radial and tangential scattering geometries, respectively. This anisotropy indicates that the weaker shear flow tended to rotate the crystallites such that the hexagonal planes were coincident with the flow-vorticity plane but did not drive the crystallites to obtain a common in-plane orientation with respect to the flow. The prolate shape of the crystallites might explain their rotation under weak shear flow, since it would lead to the long dimension of the crystallites orienting along the flow direction and the short dimension orienting along the gradient direction.

B. Nanorod ordering in nematic and hexagonal wormlike micelles.

Above $c \approx 800$ mM, CPyCl/NaSal WLMs form equilibrium phases with liquid crystalline order, including a nematic and a hexagonal phase.[25] The ordering behavior of suspended nanorods and their response to shear differs dramatically in these mesophases compared with the behavior in isotropic WLM solutions described above. Fig. 8(a) and (b) show the scattering intensity in the flow-vorticity plane under quiescent conditions and under shear at $\dot{\gamma}$ = 1 s^{-1},

respectively, from a nanorod suspension in a solution of nematic WLMs with c = 1133 mM. Unlike in isotropic WLM solutions, no evidence of ordering, such as a powder Bragg peak, developed in the quiescent solution, and the scattering pattern resembled that of well-dispersed rods with a weakly anisotropic orientation distribution. (In this case, the sample was not subject to a pre-shear at 50 s^{-1} following loading into the Couette cell, and we associate this weak anisotropy with residual alignment of the nanorods parallel to the Couette cell axis introduced during the loading that was slow to relax due to the high viscosity of the WLM solution at this concentration.) Upon application of shear, the rods were driven into an ordered arrangement; however, the nature of the ordering differed from the hexagonal order seen in the isotropic WLM solutions. As shown in Fig. 8(b), a set of peaks developed along q_v in the SAXS pattern, indicating a stacking of layers of rods. Thus, the rods under shear again assembled into layers, but the layer normal in this case was parallel to the flow direction rather than the gradient direction as in the isotropic WLMs. Further, the scattering along the vorticity direction remained diffuse, indicating liquid-like order of the rods within each layer. That is, the rods assumed a structure similar to the smectic-A phase of liquid crystals. The smectic peaks are shown in Fig. 8(c), which displays the scattering intensity along q_v at $q_\omega = 0$. Again, the plotted intensity is the intensity per pixel averaged over a ten-pixel-wide band centered at $q_\omega = 0$ and multiplied by q_v^2 to correct approximately for the form factor of rods aligned the flow direction. The peaks are spaced by $\Delta q_v \approx 0.07$ nm^{-1}, corresponding to a layer spacing of 89 nm. This spacing is larger than that obtained in the RCP assemblies that form in the isotropic WLM solutions, likely because the smectic layers did not have the same apparent inter-digitation that the hexagonal layers of the RCP structure showed. A Lorentzian fit to the first-order smectic peak, shown on an expanded scale in Fig. 8(d) along with the fit result, gives a correlation length of $\xi = 110 \pm 1$ nm. Meanwhile, the diffuse scattering along the vorticity direction is peaked at a wave-vector magnitude, $q \approx 0.283$ nm^{-1}, that corresponds to a typical nearest neighbor distance of about $2\pi/0.283 \approx 22$ nm, which is smaller than the hexagonal lattice spacing in the RCP structure, again consistent with the lack of inter-digitation by the smectic layers. The inset to Fig. 8(c) displays a schematic representation of the smectic ordering of the rods in the nematic WLM solution under shear.

At still higher CPyCl concentration, where the WLMs enter a hexagonal phase, the rods showed no ordering under either quiescent conditions or shear. For example, Fig. 9(a) and (b) display scattering patterns from a nanorod suspension in a solution with c = 1500 mM, which places the WLMs in the hexagonal phase, under quiescent conditions and during shear at $\dot{\gamma}$ = 1 s^{-1}, respectively. The pattern in Fig. 9(b) displays anisotropy consistent with alignment of the rods parallel to the flow direction, indicating the rods acquired nematic order under shear, but shows no signs of shear-induced long-range spatial correlations that would indicate ordered assembly of the rods.

IV. Discussion

As noted above, the observed self-assembly and shear-induced order among dispersions of nanorods in the WLM solutions imply an attractive interaction between rods. We note that, while the results in Fig. 2-4 showing the nanorod ordering in isotropic WLM solutions focus on solutions with c = 400 mM, effectively the same self-assembly and ordering behavior was observed at c = 220 mM. However, at the lowest CPyCl concentration in the study, c = 110 mM, the rods remained dispersed under both quiescent conditions and shear, implying that a minimum concentration of micelles is required to mediate an attractive force that is adequate to drive the assembly. Additional measurements (results not shown) on nanorod suspensions in solutions of NaSal in the absence of CPyCl at a concentration matching that of the solution with c = 400 mM found that the nanorods similarly remained dispersed, confirming that the attraction derives from the micelles and not simply from the ionic concentration of the solution. A second feature that is apparently important for the assembly is the aspect ratio of the rods. In an earlier SAXS study we investigated CPyCl/NaSal solutions containing Au nanorods that were synthesized using the identical procedure as in the present study but that had smaller length, L = 45 nm instead of 75 nm.[43] The shorter rods remained well dispersed for CPyCl concentrations up to c = 500 mM. (Evidence for nanorod assembly at higher concentration was noted in that work but was not investigated in detail.)

These dependences on micelle concentration and particle dimension indicate that the WLMs act as a depletant in creating an attractive interaction among the nanorods.[44] The

alignment and assembly of nanorods, including into hexagonal packings, in solution via depletion forces mediated by polymers or spherical micelles has been previously demonstrated.[16, 45-49] In addition, depletion forces mediated by WLMs are well documented,[27, 28] although previous examples involved colloids that were much larger than the nanorods in this study, and the resulting forces led to disordered colloidal aggregates.[27] Here, we observe how in the case of rod-like nanoparticles, semidilute WLMs can mediate depletion forces whose scale is well tuned to promote ordered assembly. We further note that since depletion forces generally depend on factors such as concentration and shape and size of the depletants relative to the interacting particles, and not chemically specific properties, the behavior seen here should be not be specific to CPyCl/NaSal but rather should be generic to the range of surfactant systems that form WLMs.

We can further understand the observed differences in nanorod ordering in the isotropic and nematic WLM solutions as a consequence of the difference in the properties of the WLMs in the two phases. In the nematic phase, where the surfactant concentration exceeds 30 wt%, steric interactions drive the micelles to form domains in which the micelles co-align, and this aligned packing increases the persistence length of the micelles. In semi-dilute polymer solutions, the range of the depletion interaction depends on the correlation length,[44] which can be expected to vary with the persistence length and other conformational properties; however, to our knowledge, depletion interactions mediated by nematically ordered macromolecules have not been previously been considered. The contrasting ordering behavior of the nanorods in the isotropic and nematic WLM solutions illustrates how these changes can have strong consequences, particularly when the depletion interaction acts between anisotropic colloids. Beyond depletion effects, however, another possible mechanism that could contribute to the attractive interactions between the nanorods in the nematic WLM solution is the nematic free energy cost imposed by the rods due to the disruption of the local nematic order. Such nematic-mediated interactions in thermotropic liquid crystals have been studied in detail,[50] but to our knowledge have not been considered in nematic WLM solutions.

V. Conclusion

In conclusion, we have demonstrated a new mechanism for the solution-based assembly of nanoparticles, specifically nanorods, into structures with order over macroscopic length scales using WLMs. A number of distinct properties of WLMs gives this approach potential advantages that are worth exploring in future studies. For example, since the WLMs used in this study are charged, their persistence length depends on the concentration of added salt. Also, the viscosity of WLM solutions shows a rapid decrease with increasing temperature that is thought to derive from a strong temperature dependence of the average micelle length. Since one can anticipate that the strength and range of the nanoparticle interaction depends on the entangled microstructure and size distribution of the WLMs, these dependences could provide facile mechanisms for tuning the interaction. Also, at micelle concentrations that are close to, but below, the concentration for nematic order, WLM solutions can display a shear-induced isotropic-to-nematic transition.[51-53] Given the different nanoparticle ordering behaviors seen in the isotropic and nematic WLM solutions described above, this transition opens the possibility of employing shear to reconfigure nanorods between different ordered structures that would interesting to explore in future studies.

Conflicts of Interest

There are no conflicts to declare.

Acknowledgements

Funding was provided by the National Science Foundation (NSF DMR-1610875). This research used resources of the Advanced Photon Source and the Center for Nanoscale Materials, U.S. Department of Energy (DOE) Office of Science User Facilities operated for the DOE Office of Science by Argonne National Laboratory under Contract No. DE-AC02-06CH11357. JL acknowledges the support from Argonne's LDRD program.

References

1. J. Zhu and M. C. Hersam, *Adv. Mater.*, 2017, **29**, 1603895.
2. Q. Zhao, C. E. Finlayson, D. R. E. Snoswell, A. Haines, C. Schäfer, P. Spahn, G. P. Hellmann, A. V. Petukhov, L. Herrmann, P. Burdet, P. A. Midgley, S. Butler, M. Mackley, Q. Guo and J. J. Baumberg, *Nature Communications*, 2016, **7**, 11661.
3. S. Sun, C. B. Murray, D. Weller, L. Folks and A. Moser, *Science*, 2000, **287**, 1989-1992.
4. Z. Nie, A. Petukhova and E. Kumacheva, *Nature Nanotechnology*, 2009, **5**, 15.
5. K. Liu, N. Zhao and E. Kumacheva, *Chem. Soc. Rev.*, 2011, **40**, 656-671.
6. R. Krahne, G. Morello, A. Figuerola, C. George, S. Deka and L. Manna, *Phys. Rep.*, 2011, **501**, 75-221.
7. P. Zijlstra, J. W. M. Chon and M. Gu, *Nature*, 2009, **459**, 410.
8. R. Kullock, W. R. Hendren, A. Hille, S. Grafström, P. R. Evans, R. J. Pollard, R. Atkinson and L. M. Eng, *Optics Express*, 2008, **16**, 21671-21681.
9. M. E. Stewart, C. R. Anderton, L. B. Thompson, J. Maria, S. K. Gray, J. A. Rogers and R. G. Nuzzo, *Chemical Reviews*, 2008, **108**, 494-521.
10. X. Huang, S. Neretina and M. A. El-Sayed, *Adv. Mater.*, 2009, **21**, 4880-4910.
11. S. Mubeen, J. Lee, N. Singh, S. Krämer, G. D. Stucky and M. Moskovits, *Nature Nanotechnology*, 2013, **8**, 247.
12. M. A. Boles, M. Engel and D. V. Talapin, *Chemical Reviews*, 2016, **116**, 11220-11289.
13. C. B. M. and, C. R. Kagan and M. G. Bawendi, *Annual Review of Materials Science*, 2000, **30**, 545-610.
14. X. Ye, L. Jin, H. Caglayan, J. Chen, G. Xing, C. Zheng, V. Doan-Nguyen, Y. Kang, N. Engheta, C. R. Kagan and C. B. Murray, *ACS Nano*, 2012, **6**, 2804-2817.
15. A.-C. Genix and J. Oberdisse, *Soft Matter*, 2018, **14**, 5161-5179.
16. D. Baranov, A. Fiore, M. van Huis, C. Giannini, A. Falqui, U. Lafont, H. Zandbergen, M. Zanella, R. Cingolani and L. Manna, *Nano Lett.*, 2010, **10**, 743-749.
17. D. Kim, W. K. Bae, S.-H. Kim and D. C. Lee, *Nano Lett.*, 2019, **19**, 963-970.
18. K. L. Young, M. L. Personick, M. Engel, P. F. Damasceno, S. N. Barnaby, R. Bleher, T. Li, S. C. Glotzer, B. Lee and C. A. Mirkin, *Angewandte Chemie International Edition*, 2013, **52**, 13980-13984.
19. M. Grzelczak, J. Vermant, E. M. Furst and L. M. Liz-Marzán, *ACS Nano*, 2010, **4**, 3591-3605.
20. Y. Min, M. Akbulut, K. Kristiansen, Y. Golan and J. Israelachvili, *Nature Mater.*, 2008, **7**, 527.
21. T. H. Besseling, M. Hermes, A. Fortini, M. Dijkstra, A. Imhof and A. van Blaaderen, *Soft Matter*, 2012, **8**, 6931-6939.
22. B. Sun and H. Sirringhaus, *Nano Lett.*, 2005, **5**, 2408-2413.
23. C. Jiang, S. M. Ng, C. W. Leung and P. W. T. Pong, *Journal of Materials Chemistry C*, 2017, **5**, 252-263.
24. C. A. Dreiss, *Soft Matter*, 2007, **3**, 956-970.
25. J. F. Berret, in *Molecular Gels: Materials with Self-Assembled Fibrillar Networks*, eds. R. G. Weiss and P. Terech, Springer Netherlands, Dordrecht, 2006, ch. 19, pp. 667-720.
26. S. Rogers, J. Kohlbrecher and M. P. Lettinga, *Soft Matter*, 2012, **8**, 7831-7839.
27. G. Petekidis, L. A. Galloway, S. U. Egelhaaf, M. E. Cates and W. C. K. Poon, *Langmuir*, 2002, **18**, 4248-4257.
28. P. Richetti and P. Kékicheff, *Phys. Rev. Lett.*, 1992, **68**, 1951-1954.
29. T. Li, A. J. Senesi and B. Lee, *Chemical Reviews*, 2016, **116**, 11128-11180.
30. F. Lehmkühler, I. Steinke, M. A. Schroer, B. Fischer, M. Sprung and G. Grübel, *The Journal of Physical Chemistry Letters*, 2017, **8**, 3581-3585.
31. T. Meins, K. Hyun, N. Dingenouts, M. Fotouhi Ardakani, B. Struth and M. Wilhelm, *Macromolecules*, 2012, **45**, 455-472.
32. H. Rehage and H. Hoffmann, *J. Phys. Chem.*, 1988, **92**, 4712-4719.

33. V. Croce, T. Cosgrove, G. Maitland, T. Hughes and G. Karlsson, *Langmuir*, 2003, **19**, 8536-8541.
34. J. Ilavsky, *J. Appl. Crystallogr.*, 2012, **45**, 324-328.
35. F. Zhang, J. Ilavsky, G. G. Long, J. P. G. Quintana, A. J. Allen and P. R. Jemian, *Metallurgical and Materials Transactions A*, 2010, **41**, 1151-1158.
36. D. Z. Gunes, R. Scirocco, J. Mewis and J. Vermant, *Journal of Non-Newtonian Fluid Mechanics*, 2008, **155**, 39-50.
37. Y. Iso, C. Cohen and D. L. Koch, *Journal of Non-Newtonian Fluid Mechanics*, 1996, **62**, 135-153.
38. L. G. Leal, *J. Fluid Mech.*, 2006, **69**, 305-337.
39. L. B. Chen, B. J. Ackerson and C. F. Zukoski, *J. Rheol.*, 1994, **38**, 193-216.
40. L. B. Chen, C. F. Zukoski, B. J. Ackerson, H. J. M. Hanley, G. C. Straty, J. Barker and C. J. Glinka, *Phys. Rev. Lett.*, 1992, **69**, 688-691.
41. J. Vermant and M. J. Solomon, *J. Phys. Condens. Matter*, 2005, **17**, R187.
42. W. Loose and B. J. Ackerson, *The Journal of Chemical Physics*, 1994, **101**, 7211-7220.
43. J. Lee, A. Grein-Iankovski, S. Narayanan and R. L. Leheny, *Macromolecules*, 2017, **50**, 406-415.
44. H. N. W. Lekkerkerker and R. Tuinier, *Colloids and the Depletion Interaction*, Springer Netherlands, Dordrecht, 2011.
45. E. Barry and Z. Dogic, *Proceedings of the National Academy of Sciences*, 2010, **107**, 10348-10353.
46. Y. Xie, S. Guo, Y. Ji, C. Guo, X. Liu, Z. Chen, X. Wu and Q. Liu, *Langmuir*, 2011, **27**, 11394-11400.
47. M. A. Modestino, E. R. Chan, A. Hexemer, J. J. Urban and R. A. Segalman, *Macromolecules*, 2011, **44**, 7364-7371.
48. R. Poling-Skutvik, J. Lee, S. Narayanan, R. Krishnamoorti and J. C. Conrad, *ACS Applied Nano Materials*, 2018, **1**, 877-885.
49. Y. Zhang and F.-M. Liu, *Appl. Surf. Sci.*, 2016, **367**, 559-562.
50. I. Musevic and M. Skarabot, *Soft Matter*, 2008, **4**, 195-199.
51. J. F. Berret, D. C. Roux, G. Porte and P. Lindner, *EPL (Europhysics Letters)*, 1994, **25**, 521.
52. E. Cappelaere, J. F. Berret, J. P. Decruppe, R. Cressely and P. Lindner, *Phys. Rev. E*, 1997, **56**, 1869-1878.
53. E. Fischer and P. T. Callaghan, *Phys. Rev. E*, 2001, **64**, 011501.

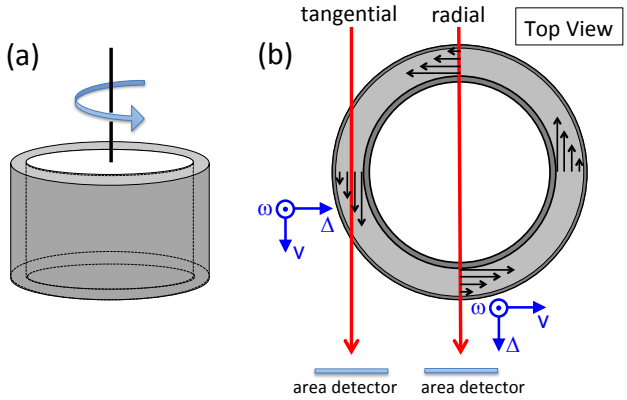

Fig. 1: Schematic representation of the experimental configurations in the Couette cell geometry. (a) The sample is contained between the outer wall of a rotating cylindrical bob with diameter 11.0 mm and the inner wall of a stationary cylinder with inner diameter 11.4 mm, leading to a sample thickness of 0.2 mm. (b) A top view illustrates with red arrows the two positions of the incident x-ray beam, radial and tangential. (Note the cell diameters and gap spacing are not to scale.) In the small-angle scattering limit, the scattering wave vector q is perpendicular to the incident wave vector, so that in the radial geometry, q is in the flow-vorticity (v-ω) plane, while in the tangential geometry it is in the gradient-vorticity (Δ-ω) plane.

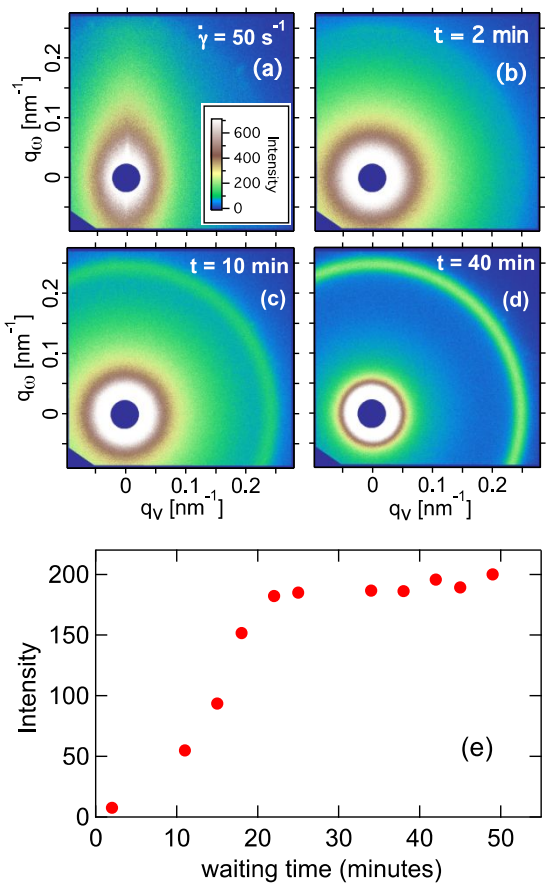

Fig. 2: SAXS patterns from a WLM solution (c = 400 mM) containing a dispersion of gold nanorods obtained (a) during shear at $\dot{\gamma}$ = 50 s^{-1} and following cessation of the shear after waiting (b) 2 minutes, (c) 10 minutes, and (d) 40 minutes. (e) Intensity of the peak near q = 0.246 nm^{-1} as a function of time after cessation of the shear.

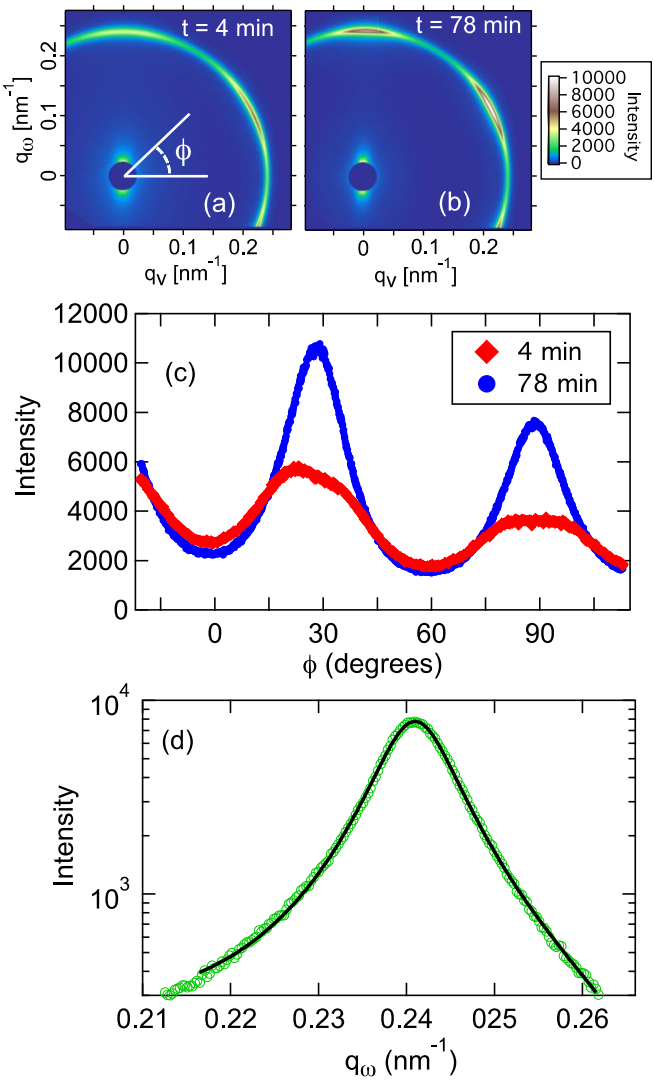

Fig. 3: (a) SAXS pattern after 4 minutes and (b) pattern after 78 minutes of shear at $\dot{\gamma} = 2.5\ s^{-1}$ obtained in the radial geometry from a WLM solution ($c = 400$ mM) containing a dispersion of gold nanorods. (c) The scattering intensity at $q = 0.24\ nm^{-1}$ as a function of the azimuthal angle ϕ after 4 minutes (red) and 78 minutes (blue) of shear. (d) Scattering intensity of the (01) peak at $\phi = 90°$ measured over a strip of width $\Delta q_v = 0.008\ nm^{-1}$ after 78 minutes of shear. The solid line is a Lorentzian fit as described in the text.

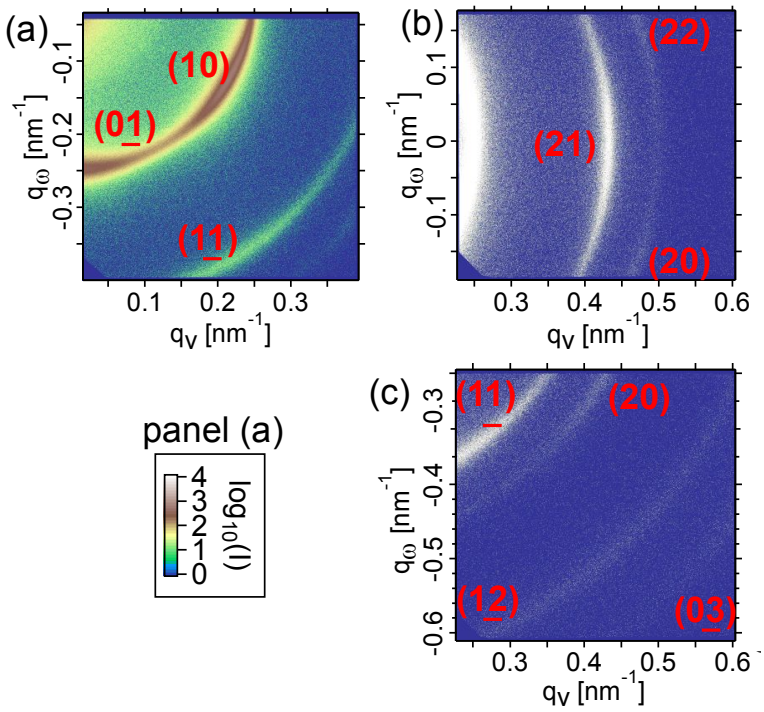

Fig. 4: SAXS patterns of gold nanorods in a WLM solution (c = 400 mM) obtained in the radial geometry with the detector positioned to capture different regions of reciprocal space. Note the color scale refers to panel (a). In panels (b) and (c) all detector pixels with non-zero intensity are shown in white. Peaks in the images are labelled according to the Miller indices for the hexagonal lattice.

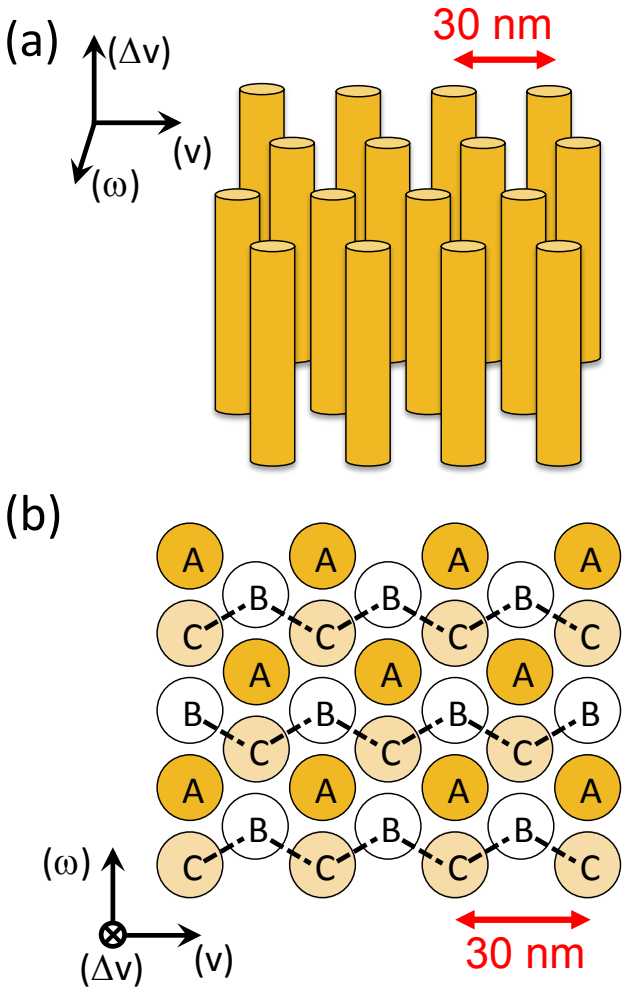

Fig. 5: (a) Schematic representation of hexagonal lattice of gold nanorods oriented by the shear flow. (b) Schematic of a reference hexagonal layer (A) in a close-packed structure oriented with respect to the flow like the gold nanorod lattices. Also shown are two possible relative positions of rods in an adjacent layer (B and C). The dashed lines indicate the directions of translation between the two sets of sites that the adjacent layers make when undergoing zig-zag strain in response to shear flow as modeled in Ref. 36.

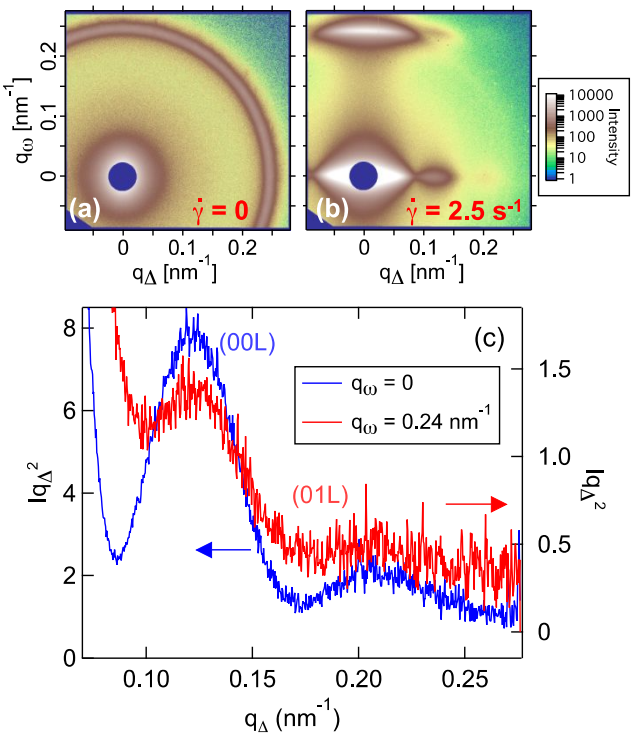

Fig. 6: SAXS pattern (a) under quiescent conditions and (b) during shear at $\dot{\gamma}$ = 2.5 s^{-1} obtained in the tangential geometry from a WLM solution (c = 400 mM) containing a dispersion of gold nanorods. (c) The scattering intensity along q_Δ, multiplied by q_Δ^2 to correct for the nanorod form factor, obtained from the pattern in (b) at q_ω = 0 (blue) and at q_ω = 0.24 nm^{-1} (red), corresponding to the (00L) and (01L) Bragg tubes, respectively.

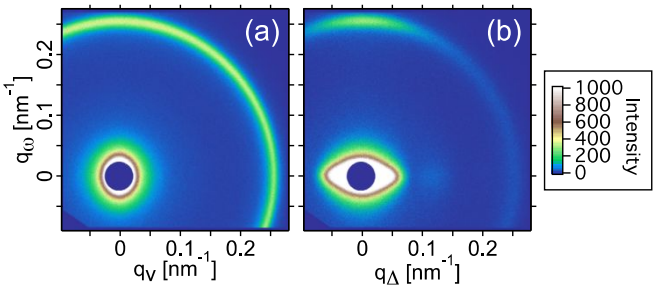

Fig. 7: SAXS patterns obtained in (a) the radial geometry and (b) the tangential geometry from a WLM solution (c = 400 mM) containing a dispersion of gold nanorods during shear at $\dot{\gamma} = 0.1\ s^{-1}$.

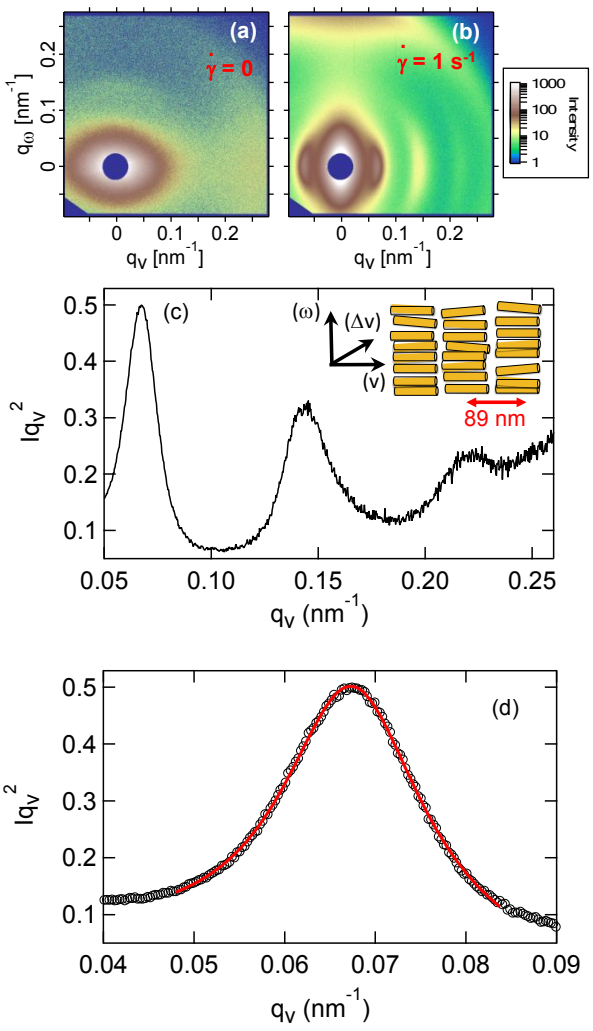

Fig. 8: SAXS pattern under (a) quiescent conditions and (b) during shear at $\dot{\gamma} = 1.0$ s^{-1} obtained in the radial geometry from a nematic WLM solution (c = 1133 mM) containing a dispersion of gold nanorods. (c) The scattering intensity along q_v at $q_\omega = 0$, multiplied by q_v^2 to correct for the nanorod form factor, obtained from the pattern in (b). (d) The first peak in the intensity from (c) on an expanded scale. The solid line is a Lorentzian fit as described in the text.

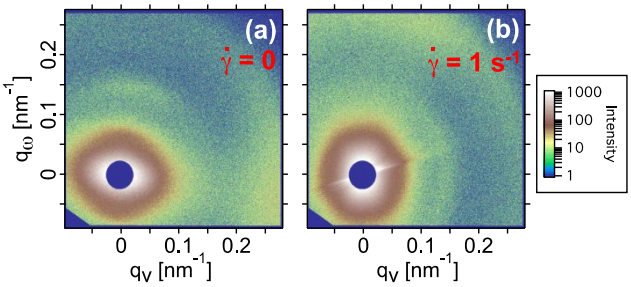

Fig. 9: SAXS pattern (a) under quiescent conditions and (b) during shear at $\dot{\gamma} = 1.0\ s^{-1}$ obtained in the radial geometry from a WLM solution in the hexagonal phase (c = 1500 mM) containing a dispersion of gold nanorods.

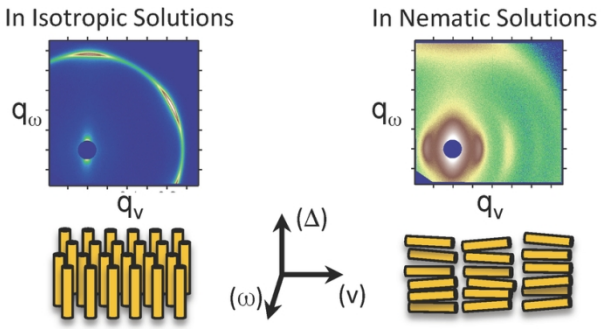

Gold nanorods in wormlike micelle solutions under shear assemble into ordered structures that depend on the micelle phase.

117x67mm (300 x 300 DPI)